The Astrophysical Journal, 740:95 (14pp), 2011 October 20 doi:10.1088/0004-637X/740/2/95

RESOLUTION OF THE COMPACT RADIO CONTINUUM SOURCES IN Arp220

Fabien Batejat[1], John E. Conway[1], Rossa Hurley[1], Rodrigo Parra[2],
Philip J. Diamond[3], Colin J. Lonsdale[4], and Carol J. Lonsdale[5]
[1] Onsala Space Observatory, SE-439 92 Onsala, Sweden; fabien.batejat@chalmers.se
[2] European Southern Observatory, Alonso de Cordova 3107, Casilla 19001, Santiago 19, Chile
[3] CSIRO Astronomy and Space Science, P.O. Box 76, Epping, NSW 1710, Australia
[4] MIT Haystack Observatory, Westford, MA, USA
[5] North American ALMA Science Center, NRAO, Charlottesville, VA, USA
Received 2011 May 18; accepted 2011 August 8; published 2011 October 4

ABSTRACT

We present 2 cm and 3.6 cm wavelength very long baseline interferometry images of the compact radio continuum sources in the nearby ultra-luminous infrared galaxy Arp220. Based on their radio spectra and variability properties, we confirm these sources to be a mixture of supernovae (SNe) and supernova remnants (SNRs). Of the 17 detected sources we resolve 7 at both wavelengths. The SNe generally only have upper size limits. In contrast all the SNRs are resolved with diameters $\geqslant 0.27$ pc. This size limit is consistent with them having just entered their Sedov phase while embedded in an interstellar medium (ISM) of density 10^4 cm^{-3}. These objects lie on the diameter–luminosity correlation for SNRs (and so also on the diameter–surface brightness relation) and extend these correlations to very small sources. The data are consistent with the relation $L \propto D^{-9/4}$. Revised equipartition arguments adjusted to a magnetic field to a relativistic particle energy density ratio of 1% combined with a reasonable synchrotron-emitting volume filling factor of 10% give estimated magnetic field strengths in the SNR shells of ~15–50 mG. The SNR shell magnetic fields are unlikely to come from compression of ambient ISM fields and must instead be internally generated. We set an upper limit of 7 mG for the ISM magnetic field. The estimated energy in relativistic particles, 2%–20% of the explosion kinetic energy, is consistent with estimates from models that fit the IR–radio correlation in compact starburst galaxies.

Key words: galaxies: individual (Arp220) – galaxies: starburst – ISM: supernova remnants

Online-only material: color figures

1. INTRODUCTION

Observations of radio supernovae (SNe) and supernova remnants (SNRs) provide an important means to study astrophysical processes occurring in dense nuclear starbursts. Radio observations of these objects are free from the dust obscuration that hamper observations at shorter wavelengths while the high angular resolution afforded by very long baseline interferometry (VLBI) observations cannot be matched by any other technique. Monitoring the rate of appearance of radio SNe can potentially constrain the stellar initial mass function and check whether it is modified in extremely dense environments such as found in Arp220 (Parra et al. 2007). The SNRs are the acceleration sites of the relativistic particles that give rise to radio emission in star-forming regions and hence their properties are central to understanding the far-IR (FIR)–radio correlation (Lacki et al. 2010). Finally, radio SNe and SNRs can be used as in situ probes to constrain the interstellar medium (ISM) properties such as density, pressure, and magnetic field strength. Recent papers dealing with VLBI observations of SNe/SNRs in starburst galaxies include Fenech et al. (2010), Lenc & Tingay (2009), Ulvestad (2009), and Pérez-Torres et al. (2009).

Arp220 is the nearest and best studied ultra-luminous infrared galaxy. For over a decade it has been the subject of a global VLBI campaign at cm wavelengths. Smith et al. (1998) made the first detection of a number of compact sub-parsec sized sources at 18 cm. These sources have been monitored and new objects discovered in successive 18 cm epochs (Rovilos et al. 2005; Lonsdale et al. 2006). Parra et al. (2007) reported the first detections of these objects at the shorter wavelengths of 13 cm, 6 cm, and 3.6 cm. Based on the source radio light curves and spectra, Parra et al. (2007) argued that the compact radio sources in Arp220 comprise a mixed population of radio SNe and SNRs.

This paper presents the results and analysis of new high sensitivity and resolution VLBI observations at 3.6 cm and 2 cm wavelengths. The main objectives of these new observations were to extend source spectra to higher frequencies, look for high-frequency variability, and most importantly attempt to spatially resolve sources or set limits on source sizes. In Section 2 we present details of the high-frequency observations and their reduction; we also describe other ancillary VLBI data used in our analysis. In Section 3 we describe our results including the source detection and resolution criteria, and the estimation of source sizes and of source spectra. In Section 4 we discuss our results and their implications for the physics of the sources and the ambient ISM. Finally in Section 5 we give our conclusions. In this paper we assume a distance of 77 Mpc to Arp220 at which an angular size of 1 mas corresponds to 0.37 pc.

2. OBSERVATIONS AND DATA REDUCTION

2.1. 3.6 cm Global VLBI

Arp220 was observed at 3.6 cm (8.4 GHz) on 2006 November 28 as part of the European VLBI Network (EVN) + Very Long Baseline Array (VLBA) global VLBI experiment GC028A. The experiment used the 10 stations of the VLBA, the Green Bank Telescope (Gb), the phased Very Large Array (VLA; Y27), Arecibo (Ar), and five EVN stations (Ef, On, Mc, Nt, Wb). The observations were performed using a dual polarization 256 Mbit s^{-1} recording mode. The data were correlated at JIVE

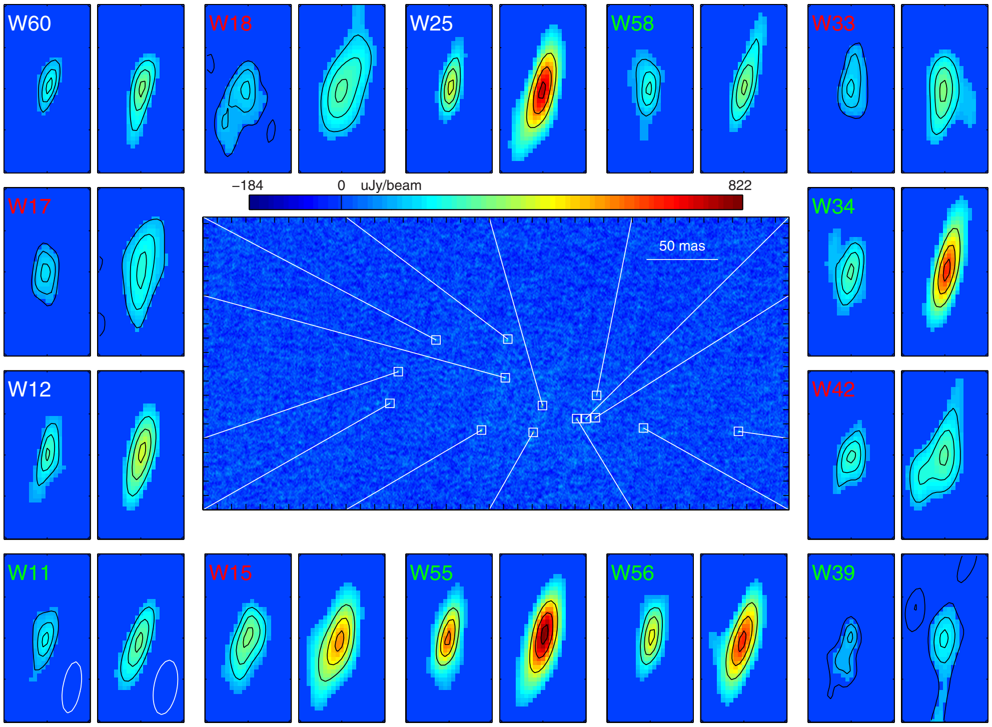

Figure 1. Central panel shows the 3.6 cm image of the western nucleus of Arp220 spanning a region 410 mas by 205 mas. Fourteen sources were detected above a 5.6σ detection threshold (see Section 3.1) at both 2 cm and 3.6 cm. The surrounding panels show zoomed images of these sources at 2 cm (left panels) and at 3.6 cm (right panels). The same color bar is used for the central panel and all zoomed images at both 2 cm and 3.6 cm. Each zoomed image covers a region of 2.1 mas by 4.1 mas. The source number is displayed in the top left corner of the 2 cm zoomed image. Where the source number is displayed in red this means that the source is resolved at both 2 cm and 3.6 cm. A green number means resolved at 2 cm only, a cyan number means resolved at 3.6 cm only, while a white number means unresolved at both 2 cm and 3.6 cm. For more information about how resolution was determined see Section 3.2.1. The zoomed images are blanked at the 3σ level and contour levels are shown at 50%, 75%, and 95% of the peak intensity of each source (given in Table 2). The 50% contour of the CLEAN restoring beam (see Table 1) at each wavelength is shown in the bottom left zoomed image.

(A color version of this figure is available in the online journal.)

in the Netherlands in a single pass using a phase center between the two nuclei and high spectral and time resolution to allow wide-field imaging. Unfortunately, no fringes were detected at the Green Bank Telescope which significantly reduced the sensitivity of the observations. Also due to a scheduling error at the station, Ar was only available for a very small fraction of the time.

The data were reduced using AIPS in a standard manner. Initial amplitude calibration was carried out using monitored system temperatures and station gains. We estimate that absolute amplitude calibration should be accurate to ∼5%. The main phase calibrator was the nearby (0°.5 separation) source J1532+2344 which was observed in a rapid switching cycle with Arp220. Simultaneous CLEAN images of size 4096 pixels × 2048 pixels (pixel spacing 0.1 mas) were then made of the eastern and western nuclei using robust data weighting to give a good compromise between sensitivity and resolution. Using the initial phase-referencing phase calibration it was found impossible to make thermal noise-limited images. To improve the dynamic range we performed phase self-calibration on the Arp220 data itself using long solution times (≈30 minutes) to obtain sufficient signal to noise. The resulting slowly varying phase solutions were consistent with unmodeled atmosphere delays differentially affecting target and calibrator. Finally, CLEAN was applied again and noise-limited images produced (see Table 1). The final images are shown in the central panels of Figures 1 and 2, with inset panels showing detailed images of individual sources. In the rest of this paper we refer to experiment GC028A when mentioning the 3.6 cm data or image if not otherwise specified.

Table 1
High Frequency VLBI Observations of Arp220

Epoch	Code	λ (cm)	Array	$\sigma_{\rm rms}$ (μJy beam^{-1})	Beam Size (mas^2)
2006.02	BP129	13.26	VLBA	129.54	3.6 × 6.6
		6.02[a]		41.43	1.8 × 3.5
		3.56		86.73	1.7 × 3.1
2006.91	GC028A	3.56	Global VLBI	34.7	0.56 × 1.34
2006.99	GC028B	2	HSA	28.12	0.43 × 1.26
2008.44	GC031A	6.02	Global VLBI	12.58	0.72 × 2.1

Note. [a] Re-reduced 6 cm observations from experiment BP129.

2.2. 2 cm HSA

Arp220 was observed at 2 cm (15 GHz) in a full track observation on 2006 December 28 using the High Sensitivity Array (HSA; expt GC028B). The experiment used the 10 stations of the VLBA, Gb, Y27, and the Effelsberg (Eb) antenna. The observations were performed in a 256 Mbit s^{-1} dual polarization mode. The data were correlated in Socorro, NM in one pass with a single phase center located midway between the two nuclei and high spectral and time resolution to allow wide-field imaging. The data were reduced using AIPS in a standard way similar to that described in Section 2.1. After

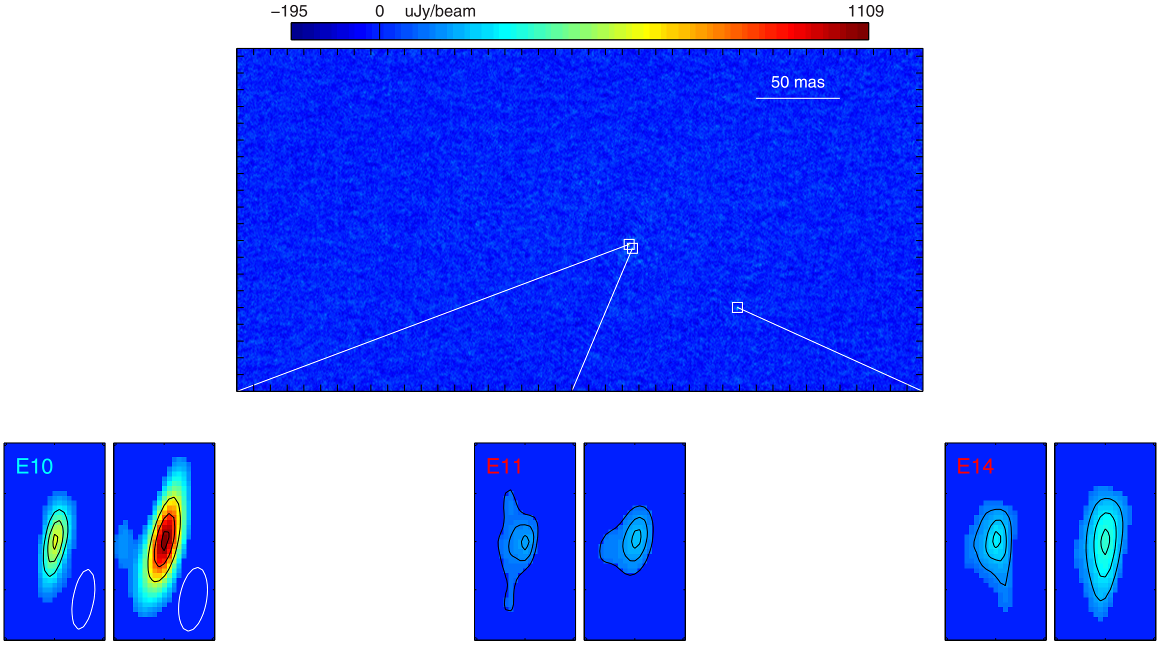

Figure 2. Central panel shows the 3.6 cm image of the eastern nucleus of Arp220 spanning a region 410 mas by 205 mas. Three sources were detected above a 5.6σ detection threshold (see Section 3.1) at both 2 cm and 3.6 cm. For information on labeling, contours, and other image properties see Figure 1.

(A color version of this figure is available in the online journal.)

experimentation with many uv data weighting schemes pure natural weighting of the visibility data was chosen. This choice gave the highest possible sensitivity at the expense of resolution; however, for other choices most sources were not detectable. As for our 3.6 cm wavelength data, phase self-calibration of the Arp220 data was required to achieve a thermal noise-limited image (see Table 1). Our resulting 2 cm wavelength images for individual sources in each nucleus are shown in insets in Figures 1 and 2, respectively.

2.3. Other VLBI Data

A number of ancillary VLBI data sets, providing multifrequency monitoring information, were also used in the analysis presented in this paper. These observations were used to primarily classify sources as SNe or SNRs (see Section 4.1). A full presentation of these monitoring data, including data on many sources only detected at lower frequency, will be given in a future paper (F. Batejat et al. 2012, in preparation).

The most extensive monitoring data exist at 18 cm wavelength where a total of nine epochs spanning from 1994.87 to 2006.43 have been observed and reduced. These data provide information on source long wavelength variability on decade timescales. We have reanalyzed the complete 18 cm data set in a consistent fashion carefully correcting for epoch-dependent variations in flux scale. Additionally to this, shorter wavelength variability can be searched for by comparing the results at 6 cm from epoch 2006.02 (experiment BP129; see Parra et al. 2007) re-reduced by us in order to achieve a lower $\sigma_{\rm rms}$ (see Table 2 for the new flux densities) with data 2.42 years later at epoch 2008.44 from a recently reduced observation (experiment GC031A, see Table 1). This latter epoch is one of a series of 6 cm monitoring experiments which we are presently reducing. Finally, we compare our new GC028A 3.6 cm data with data from Parra et al. (2007) taken 0.9 years earlier. Because of the low SNR of this old 3.6 cm wavelength data, it has not been possible to re-reduce it using self-calibration techniques (unlike 6 cm data from the same experiment).

3. RESULTS AND ANALYSIS

3.1. Source Detection

Visual inspection of the final 2 cm and 3.6 cm images (Figures 1 and 2) shows many sources clearly visible at both wavelengths. To more rigorously define a list of detected sources we applied a two-pass search method as used by Parra et al. (2007). First the whole east and west nucleus images were searched for sources significantly above the noise, using a detection limit which minimized the chance of false detections. Then, in a second pass, small regions were searched around the positions of known sources (previously detected at 18 cm, 6 cm, and 3.6 cm since the first detection of compact sources by Smith et al. 1998) using a lower detection threshold. For a detection limit set to $\eta\sigma$ where σ is the noise rms, the probability of one or more false detections in an image is $F = 1 - P(I < \eta\sigma)^{N_s}$, where $P(I < \eta\sigma)$ is the cumulative probability of a noise spike at a given beam area being less than $\eta\sigma$ and N_s is the number of beam areas searched. Histograms of the pixel values in source-free areas at both wavelengths were close to Gaussian out to the most extreme pixel values, hence P could be calculated assuming Gaussian statistics. In both passes we chose η such that F was 0.2%. Given that we have two passes and two wavelengths, this choice gave a final probability of <1% of getting one or more false detections.

For the first pass, given the number of beam areas at 2 cm, the above chosen value of F corresponded to $\eta = 5.6$. Although the number of searched beams was slightly less at 3.6 cm wavelength we conservatively used the same detection criteria. This first pass applied separately to both wavelengths resulted in the detection of 14 sources in the western nucleus (two of which, namely, W58 and W60, were new detections) and 3 in the eastern nucleus. All of these sources were detected at both

Table 2
Position of Detected Radio Sources and Flux Densities

Name (1)	SN (2)	α_{2000} $15^{\rm h}34^{\rm m}$... (3)	δ_{2000} $23°30'$... (4)	BP129 13 cm Peak (μJy beam^{-1}) (5)	BP129 6 cm Peak (μJy beam^{-1}) (6)	GC031A 6 cm Peak (μJy beam^{-1}) (7)	BP129 3.6 cm Peak (μJy beam^{-1}) (8)	GC028A 3.6 cm Peak (μJy beam^{-1}) (9)	GC028A 3.6 cm Integrated (μJy) (10)	GC028B 2 cm Peak (μJy beam^{-1}) (11)	GC028B 2 cm Integrated (μJy) (12)
Error (σ)				±130	±41	±13	±87	±35	±35	±28	±28
W11	...	$57^{\rm s}.2299$	$11''.502$	573	581	818	357	289	279	190	163
W12	...	$57^{\rm s}.2295$	$11''.524$	1011	711	953	341	389	416	258	253
W15	...	$57^{\rm s}.2253$	$11''.483$	579	959	1115	707	546	837	314	500
W17	6	$57^{\rm s}.2241$	$11''.520$	477	524	454	484	218	385	150	134
W18	7	$57^{\rm s}.2240$	$11''.547$	559	834	738	451	272	560	156	288
W25	...	$57^{\rm s}.2222$	$11''.501$	1069	1141	1479	648	752	965	390	324
W33	11	$57^{\rm s}.2200$	$11''.491$	582	417	321	397	310	409	162	182
W34	...	$57^{\rm s}.2195$	$11''.492$	699	1066	1458	743	650	758	263	358
W39	12	$57^{\rm s}.2171$	$11''.485$	749	428	466	120	190	247	129	91
W42	13	$57^{\rm s}.2122$	$11''.482$	743	693	706	574*	273	492	240	251
W55	...	$57^{\rm s}.2227$	$11''.482$	124	1000	569	1147	822	1001	595	693
W56	...	$57^{\rm s}.2205$	$11''.491$	...	905	1434	750	657	815	426	446
W58	...	$57^{\rm s}.2194$	$11''.508$	...	408	723	...	322	296	226	250
W60	...	$57^{\rm s}.2276$	$11''.546$	...	285	1016	...	310	268	200	128
E10	...	$57^{\rm s}.2915$	$11''.335$	227	1034	1631	988	1109	1394	577	596
E11	...	$57^{\rm s}.2913$	$11''.333$	...	429	310	...	201	171	165	195
E14	...	$57^{\rm s}.2868$	$11''.298$	...	698	608	549	343	509	264	400

Notes. Col. (1): source name from Lonsdale et al. (2006) for all sources except W55 and W56, which are from Parra et al. (2007). Sources W58 and W60 are newly detected sources. W indicates the source is located in the western nucleus while E stands for east. Col. (2): name used in Smith et al. (1998) and Rovilos et al. (2005). Cols. (3) and (4): J2000 right ascension and declination obtained by fitting a Gaussian to the sources in the highest frequency map (2 cm map). Col. (5): 13 cm peak flux density from the observations performed in experiment BP129 and presented in Parra et al. (2007). Col. (6): re-reduced 6 cm peak flux density from experiment BP129. Re-working of these data allowed us to produce a deeper map of both nuclei with $\sigma_{\rm rms} = 41.43\,\mu$Jy beam^{-1} and to detect two more sources in the western nucleus (W58 and W60) and one more source in the eastern nucleus (E11). Col. (7): newly acquired (epoch 2008.44) 6 cm peak flux density which will be presented and discussed in detail in F. Batejat et al. (2012, in preparation). Col. (8): 3.6 cm peak flux density from the observations performed in experiment BP129 and presented in Parra et al. (2007). For source W42 (marked by an asterisk) we give the integrated flux density because this source appeared resolved. Cols. (9) and (10): 3.6 cm peak and integrated flux densities from experiment GC028A discussed in this paper. Cols. (11) and (12): 2 cm peak and integrated flux densities from experiment GC028B discussed in this paper.

wavelengths. In the second pass the search regions were limited to boxes of 4 mas^2 centered on the positions of known sources. Given the smaller number of beam areas searched in this pass the critical detection threshold was smaller ($\eta = 3.8$). Despite this lower limit no additional detections were made.

Table 2 gives the absolute positions of the 17 detected sources, estimated by fitting a Gaussian to the 2 cm image of each source. Given the relatively close-by calibrator source used ($0^\circ.5$ distant) the absolute astrometric accuracy is likely limited (Pradel et al. 2006) by the accuracy of the phase calibrator position (estimated for J1532+234 to be 0.5 mas; Petrov et al. 2005). In Table 2 we therefore give positions rounded to the nearest milliarcsecond in each coordinate. Columns 9–12 of Table 2 give source peak and total flux densities at 3.6 cm and 2 cm from experiments GC028A and B. The total flux densities were measured within a tight box surrounding each source. For other epochs and wavelengths (Columns 5–8) only peak flux densities are given; since however sources are unresolved in these data, peak brightness measurements should also be good estimates of source total flux densities. Note that the 6 cm flux density values given for BP129 in Table 2 are based on a re-reduction of the data using self-calibration while the values at other wavelengths are taken from Parra et al. (2007). For the re-reduced 6 cm data source flux densities are on average a factor of 1.36 larger than found by Parra et al. (2007); this increase is likely due to an increase in phase coherence of that data. A possible slight overestimate in flux densities due to noise biasing of low SNR self-calibrated data potentially could also be present but this potential effect is hard to quantify without detailed simulations.

3.2. *Size Estimation*

A primary goal of our new high-frequency observations was to measure or set limits on the source sizes. From visual inspection of the inset images in Figures 1 and 2, there are several candidate-resolved sources (i.e., W18, W33, W42, and E14) where the 50% of peak contour, at least at one wavelength, encloses a significantly larger area than the beam and so appear resolved. Quantitative tests are, however, required to confirm or reject these visual impressions and to give size estimates with confidence limits. Two methods were developed to do this. In the method described in Section 3.2.1 we tested whether the null hypothesis that a source was unresolved could be rejected while in Section 3.2.2 we describe a procedure applied to give best estimates (with error bars) of each source's size. In Section 3.2.3 we summarize the results obtained after applying these methods to our data.

3.2.1. *Test of Resolution*

We tested whether or not each source was consistent with the null hypothesis of a point source convolved with the CLEAN Gaussian restoring beam (having minor and major axis dispersions of $\sigma_{\rm x}$ and $\sigma_{\rm y}$). For each source we calculated an

Table 3
Source Resolution Probabilities and Size Estimates

Source	2 cm	3.6 cm	Radius 2 cm (mas)			Radius 3.6 cm (mas)			Radius	Diameter	Source ID
	(%)	(%)	Mean	Min	Max	Mean	Min	Max	(mas)	(pc)	
(1)	(2)	(3)	(4)	(5)	(6)	(7)	(8)	(9)	(10)	(11)	(12)
W11	95.2	68.8	0.258	0.142	0.362	. . .	. . .	0.331	0.26	0.19	SN
W12	88.4	24.8	. . .	. . .	0.274	. . .	. . .	0.201	<0.28	<0.21	T
W15	99.8	98.5	0.358	0.310	0.418	0.409	0.308	0.502	**0.38**	**0.28**	SNR
W17	96.3	90.5	0.324	0.202	0.444	0.410	0.207	0.584	**0.37**	**0.27**	SNR
W18	99.9	98.1	0.527	0.421	0.629	0.486	0.328	0.616	**0.51**	**0.38**	SNR
W25	33.0	72.4	. . .	. . .	0.138	. . .	. . .	0.285	<0.29	<0.22	T
W33	96.6	97.9	0.317	0.205	0.429	0.472	0.320	0.596	**0.39**	**0.29**	SNR
W34	99.9	4.8	0.444*	0.372*	0.506*	. . .	. . .	0.100	. . .	. . .	SN
W39	92.7	69.3	0.309	0.138	0.472	. . .	. . .	0.501	0.31	0.23	U
W42	98.2	99.1	0.305	0.225	0.372	0.544	0.415	0.672	**0.42**	**0.31**	SNR
W55	97.7	43.4	0.202	0.145	0.229	. . .	. . .	0.209	0.20	0.15	SN
W56	92.5	87.0	0.177	0.100	0.226	. . .	. . .	0.327	0.18	0.13	SN
W58	99.8	10.9	0.389*	0.317*	0.450*	. . .	. . .	0.101	. . .	. . .	SN
W60	64.3	9.8	. . .	. . .	0.234	. . .	. . .	0.100	<0.24	<0.18	SN
E10	83.1	97.6	. . .	. . .	0.204	0.280	0.224	0.328	0.28	0.21	U
E11	99.5	97.4	0.482	0.367	0.585	0.500	0.327	0.656	**0.49**	**0.36**	SNR
E14	99.8	95.8	0.460	0.390	0.519	0.363	0.227	0.475	**0.41**	**0.30**	SN

Notes. Col. (1): source name from Lonsdale et al. (2006) for all sources except W55 and W56, which are from Parra et al. (2007). Sources W58 and W60 are newly detected sources. Cols. (2) and (3): probability (P) of source being resolved at 2 cm and 3.6 cm, respectively, using the method described in Section 3.2.1. We classify a source as provisionally resolved at that frequency in cases $P \geqslant 90\%$. Cols. (4)–(6): the mean, minimum, and maximum outer shell radii at 2 cm (experiment GC028B) as calculated by the algorithm described in Section 3.2.2. In cases where a source is unresolved only an upper limit is given, i.e., a max value. Cols. (7)–(9): the mean, minimum, and maximum outer shell radii at 3.6 cm (experiment GC028A) as calculated by the algorithm described in Section 3.2.2. In cases where a source is unresolved only an upper limit is given, i.e., a max value. Col. (10): best estimate of outer shell radius. In cases where the source is resolved at both bands this is calculated by averaging the values of Columns 4 + 7 in mas and the result is printed in bold font. Where a source is resolved only at one band the radius is given as the mean value of the resolved band. Where a source is unresolved at both bands, the radius is given as an upper limit taken as the bigger of the two max values. Col. (11): outer shell diameter in parsecs. Col. (12): source identification; SN = supernova, SNR = supernova remnant, T = transition candidate, U = unclassified (see the Appendix). The * beside the 2 cm size estimates for W34 and W58 indicate that we consider these unreliable (see Section 3.2.3) and we therefore do not list a size for these sources in Columns 10 and 11.

observed minor axis dispersion $\sigma_{x_{\rm obs}}$ from

$$\sigma^2_{x_{\rm obs}} = \frac{\iint I(x, y)\Delta x^2 dx dy}{\iint I(x, y) dx dy}, \tag{1}$$

where Δx is measured along the minor axis through the source center. If, given the expected noise, $\sigma_{x_{\rm obs}}$ was significantly larger than σ_x the point-source hypothesis was rejected. Analytic calculation of how much the former quantity must exceed the latter to be confident of resolution is difficult, first because of pixel-to-pixel correlations in noise, and second because of blanking applied to the data. Any practical method of estimating $\sigma_{x_{\rm obs}}$ must first blank the image $I(x, y)$ below say, $3\sigma_{\rm rms}$ or else the statistic is dominated by distant noise peaks. This blanking however makes the problem nonlinear.

To circumvent the above problems we applied a statistical bootstrapping technique. For each detected source a point of the same flux density convolved with the restoring beam was added at multiple (source-free) positions on the final image to test the effect of different realizations of the noise. Each realization was blanked below $3\sigma_{\rm rms}$ and the minor axis spatial dispersion $\sigma_{x_{\rm obs}}$ measured. The resulting histogram of measured dispersion values was then compared to that measured for the source using the same blanking criteria. If this latter quantity was greater than 90% of the histogram values the null hypothesis of a point source was provisionally rejected.

Table 3 lists for each source and wavelength the percentage probability of the point-source hypothesis being rejected. According to our adopted criteria of 90% confidence 13 sources are provisionally resolved at 2 cm and 8 at 3.6 cm. In total seven sources fulfill our resolution criterion at both bands. Since all these have <1% cumulative probability of achieving their measured dispersion by chance if a point source we argue that for these sources the point-source hypothesis can be rejected.

3.2.2. Estimating Source Sizes

Best estimates of source sizes with error bars were made using a variation on the method presented in Section 3.2.1. Again we added a model source to the final image at multiple positions to take into account different realizations of the noise. In this case however the model added was a spherical shell convolved with the CLEAN restoring beam, whose outer diameter we then adjusted at each position until the measured dispersion after blanking equaled the observed source dispersion after blanking. At positions where even a source of zero size was unable to produce a minor axis dispersion small enough to equal that measured from the data we set the estimated source size to zero. The SNR shell model used had a ratio of inner to outer diameter 0.8 similar to that measured for SN1993J (Martí-Vidal et al. 2011) and SN2008iz (Brunthaler et al. 2010) and consistent with the observation of evolved SNRs in M82 (Kronberg et al. 1985; Muxlow et al. 1994; Beswick et al. 2006; Fenech et al. 2008, 2010). From the resulting histogram of outer shell diameters we then obtained a best estimate of the source size and estimated error bars. In some cases we obtained good fits for the outer diameter (>0) in over 90% of realizations. In these cases we took the best estimate of source size as the mean of the histogram over all realizations with failed solutions set to zero size and

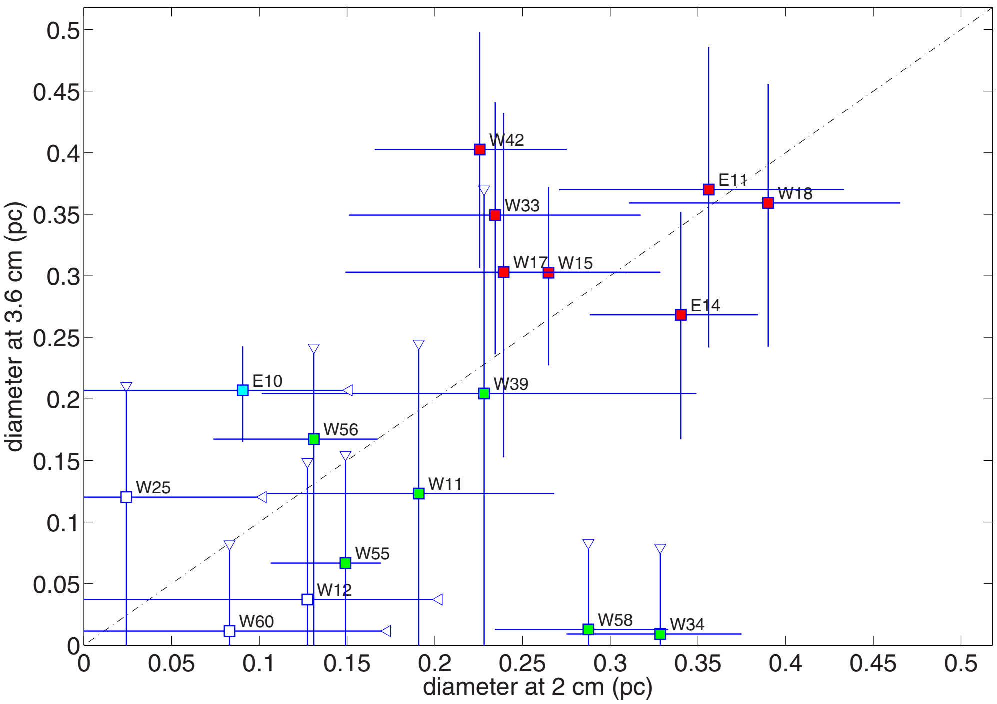

Figure 3. Plot of estimated source outer shell diameters at 2 cm and 3.6 cm. The estimated source sizes and error bars at each wavelength are assigned as described in Section 3.2.2. Symbol color indicates the results of source resolution testing described in Section 3.2.1. Red indicates that the source is resolved at both 2 and 3.6 cm defined as 99% confidence rejection of the null hypothesis that the source is a point. Green means that the source is provisionally resolved at 2 cm only and cyan that the source is provisionally resolved at 3.6 cm only. White represents sources that are unresolved at both bands.

(A color version of this figure is available in the online journal.)

defined error bars from its 10th and 90th percentiles. In other cases with <90% of realizations giving good solutions we still set a size upper limit at the 90th percentile of fitted sizes but we set the lower limit to zero.

3.2.3. Summary of Results for Source Resolution/Size

The results of the statistical tests described in Sections 3.2.1 and 3.2.2 are summarized in Figure 3. Three sources (W12, W25, and W60) are very compact and unresolved at both wavelengths, using both resolution/size estimation methods. This demonstrates that residual atmospheric phase errors do not have any appreciable effect in broadening our sources, since such errors would affect all sources. Seven sources (E10, W11, W34, W39, W55, W56, and W58) are provisionally resolved at one wavelength (usually 2 cm) and a further seven sources (E11, E14, W15, W17, W18, W33, and W42) are resolved at both wavelengths. All of the latter group have diameters greater than 0.7 mas.

Figure 3 shows in general a strong correlation between the sizes/limits measured at the two bands. Two clear exceptions, however, are W34 and W58, both of which are well resolved at 2 cm but are unresolved at 3.6 cm. Inspection of the detailed image for W34 at 2 cm shows that an isolated probable noise feature to the northwest gets through the initial 3σ blanking and contributes to a large minor axis spatial dispersion. The case of W58 is less clear since there is no distinct peak off the main source just a broadened source with position angle different to the CLEAN beam. This could, however, be caused by a large noise peak that lies very close or on top of the source. The presence of one or two such anomalous sources is not unexpected by chance given the blanking method used. There are 17 sources each at two frequencies with approximately 10 independent beam areas per source box in Figures 1 and 2. Given this total area there is a probability of 37% of detecting one or more such $> 3\sigma$ noise peaks and a 8% chance of detecting two or more such peaks.

It should be noted that although well resolved at both bands both W42 and W33 seem to be significantly larger at 3.6 cm than 2 cm; possible explanations for this are discussed in Section 4.2. In addition the estimated size of W42 at 3.6 cm in GC028A (ring outer diameter 0.82 mas) is much less than that claimed at the same frequency by Parra et al. (2007) from earlier BP129 VLBA observations (equivalent to an outer shell diameter of 3.6 mas after converting from the fitted Gaussian FWHM). It should be noted that the beam area of these earlier VLBA observations was much larger, by a factor of six, compared to our new global 3.6 cm observations. A consequence is that a shell of the size and brightness claimed from the BP129 observations would be below the thermal noise per beam of full resolution GC028A data and so would be undetectable. To check this possibility lower resolution versions of the GC028A images and recent very sensitive global 6 cm observations (GC031A) were inspected but neither were consistent with the large shell structure claimed from the BP129 3.6 cm data.

The initial argument for the resolution of W42 at 3.6 cm in Parra et al. (2007) was based on having two large VLBA beams areas above 50% of the peak source brightness. Significant residual atmospheric phase errors in the data (expected to be larger than those known to be present at 6 cm) may have contributed to an apparent source broadening, unfortunately the SNR is too low at 3.6 cm to allow self-calibration reprocessing of the BP129 to quantify atmospheric broadening at this wavelength. Residual phase errors at 3.6 cm would have broadened all sources equally but when combined with the low surface brightness of W42 this might explain the BP129 result. From these data the 50% of peak contour level is only three times

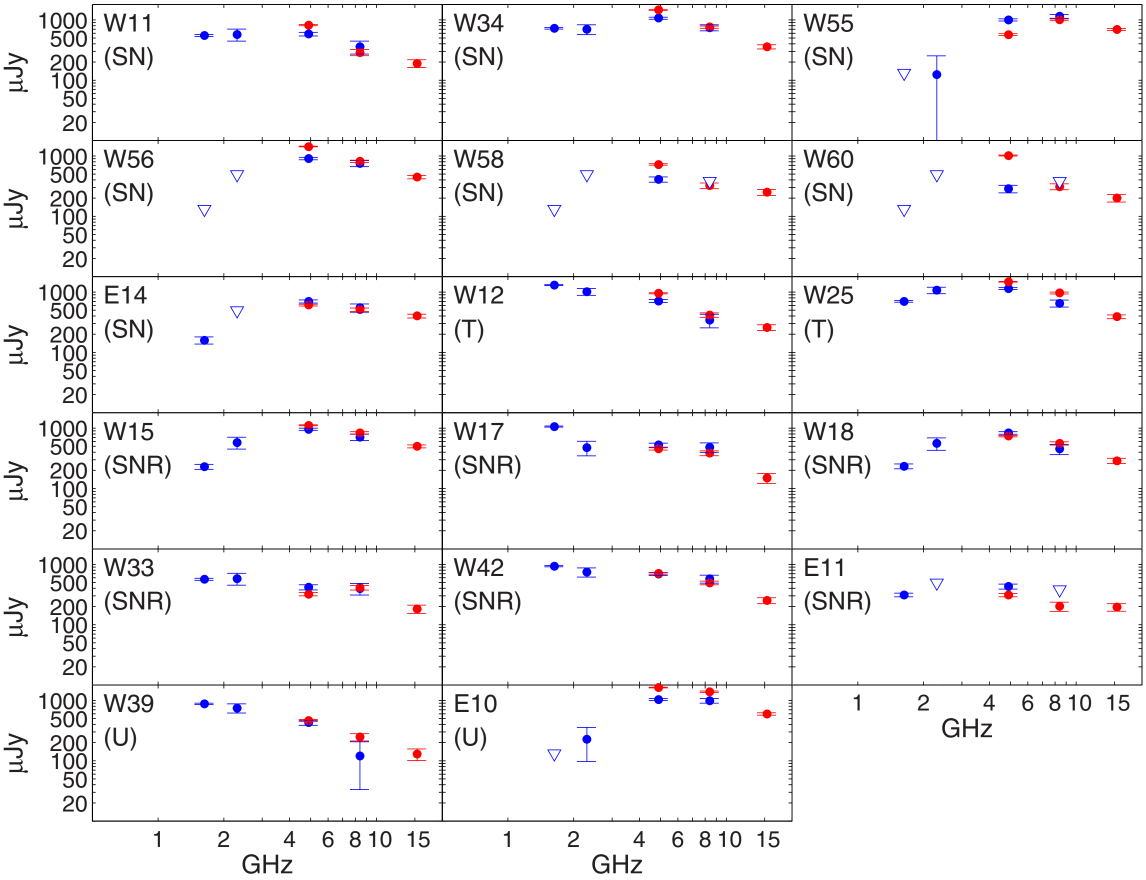

Figure 4. Spectra for the sources detected at 2 cm and 3.6 cm. Blue points are from measurements taken in time period 2006.02–2006.43 and red points in time period 2006.91–2008.44. Error bars are plotted at $\pm 1\sigma$. In case of non-detections upper limits are shown as triangles. At 18 cm (1.7 GHz), 13 cm (2.3 GHz), and 3.6 cm (8.4 GHz) upper limits are shown at upper limits of 6σ, 3.8σ, and 4.4σ, respectively (see Section 3.1; Parra et al. 2007). The blue data points at 13 cm and at 3.6 cm were taken from simultaneous observations in BP129. The blue points at 6 cm (5 GHz) are taken from new reduction of BP129 observations. The new 6 cm, 3.6 cm, and 2 cm (15 GHz) points are plotted in red. The 18 cm data are from unpublished experiment GD21A (epoch 2006.43). The spectra are grouped according to the classification scheme discussed in Section 4.1 where SN = supernova, T = transition object, SNR = supernova remnant, and U = unclassified. For unresolved sources we adopt the measured peak brightness per beam as the best estimate of the total flux density to plot while for resolved sources we plot the integrated flux density within a tight box surrounding the source.

(A color version of this figure is available in the online journal.)

the rms of the thermal noise (see Parra et al. 2007, Figure 4). Given there were a total of 18 sources detected by Parra et al. (2007) the probability of at least one of them having a 3σ noise peak adjacent to the source, so giving the impression of a highly resolved source, is not negligible (2.5%) and furthermore this probability of false resolution would increase rapidly in the presence of even a moderate amount of atmospheric source broadening.

3.3. *Source Spectra*

The short wavelength observations presented in this paper allow us to extend the source radio spectra first studied by Parra et al. (2007) to higher frequency (15 GHz, 2 cm). In addition the 3.6 cm observations and new 6 cm observations (see Table 1) can be compared to those in Parra et al. (2007) to look for high-frequency variability. Both spectral shapes and variability are useful diagnostics when attempting to classify sources as SNRs or SNe (see the Appendix). Figure 4 shows the source spectra with the points measured in the period 2006.02–2006.43 plotted in blue and those observed in the period 2006.91–2008.44 plotted in red. The measured flux densities at each epoch are taken from Table 2.

4. DISCUSSION

4.1. *Source Properties and Identification*

Parra et al. (2007) argued that the compact radio sources in Arp220 comprise a mixed population of SNe and SNRs; the former embedded in an ionized circumstellar bubble and the latter strongly interacting with the surrounding ISM. In addition to the above two classes SN/SNR “transition” objects may also exist in which ISM interaction has begun but the swept up mass is less than the ejecta mass. Other compact sources might be associated with active galactic nuclei (AGNs). Below we discuss the expected properties and likely members of each class. The Appendix gives a description of the variability and spectral properties for each source and its classification.

Supernovae. In these objects the synchrotron-emitting blast wave transits the dense circumstellar medium of the progenitor star, originating from a pre-explosion stellar wind with a r^{-2} density profile, which is ionized by the SN explosion. As the SN expands the competition between fading synchrotron emission from the emitting shell and decreasing free–free optical depth gives a characteristic light curve with a relatively fast rise followed by a gradual decline, with the peak flux density occurring later at longer wavelengths. Those of our sources which have had rapid rises in flux density at 18 cm and stable or decreasing flux densities at shorter wavelengths are almost certainly radio SNe. The expected radio spectra of such sources is a power law with a sharp cutoff toward long wavelengths. While foreground ionized ISM can also cause low-frequency turnovers in SNR sources these turnovers are expected only at frequencies $\leqslant$ 2 GHz (Parra et al. 2007), hence sources with turnovers at a higher frequency are most likely SNe. Based on the above light curve and spectrum criteria in the Appendix we provisionally classify W11, W34, W55, W56, W58, W60, and E14 as radio SNe.

Transition objects. When the SN blast wave reaches the boundary of the wind-blown bubble it starts to interact with the constant density ISM. This boundary is determined by the balance between wind ram pressure and ISM static pressure. As the shock wave propagates outward dense shocked ISM gas is accreted, relativistic particles are efficiently accelerated and the magnetic field is amplified (Berezhko & Völk 2004) causing the source to brighten simultaneously at all radio frequencies. This transition phase lasts approximately until the swept up mass equals the ejecta mass and the source enters its SNR Sedov phase. In our data W12 and W25 have rising light curves at multiple wavelengths and are therefore candidate objects of this type.

A similar increase in flux density at all radio wavelengths has been observed in SN1987A in the Large Magellanic Cloud (LMC; Zanardo et al. 2010). Even though similar to the radio brightening expected in sources in which the blast wave starts to interact with the dense ISM, in the case of SN1987A it is thought that the SN blast wave has started to interact with a dense ring of gas emitted by the progenitor star 20,000 years before the explosion (Burrows et al. 1995). Hydrodynamic modeling suggests that the dense ring was emitted during the merger of two stars (Morris & Podsiadlowski 2007). It is possible that the potential "transition sources" in Arp220 also arise from a similar mechanism. Although such merger events must be rare in most galaxies they may be more common in the dense stellar environment of Arp220.

Supernova remnants. When the shock created in an SN explosion has swept up an ISM mass equal to the ejecta mass the source enters the Sedov phase of SNR evolution. In the early part of this phase the total energy in relativistic particles stays approximately constant (Berezhko & Völk 2004). In models where the internal shell magnetic field comes from shock compressed external ISM field (van der Laan 1962; Thompson et al. 2009) the internal magnetic field is close to constant as the source expands and hence the radio luminosity is also constant. In contrast for models in which the magnetic field is internally amplified (Berezhko & Völk 2004), the magnetic energy density decreases and so does the radio luminosity. A constant or falling flux density at all wavelengths is an expected signature of a radio SNR. In addition, since the SNR shell is propagating through mainly neutral ISM local free–free absorption effects should be small and the radio spectrum close to a power law. Although free–free absorption from foreground ionized ISM can occur, this is likely to happen only at frequencies $\leqslant$ 2 GHz (Parra et al. 2007). In the Appendix we classify sources W15, W17, W18, W33, W42, and E11 as likely SNRs based on the above expected properties. Most of these sources show relatively flat ($\alpha < 0.5$) spectra from 18 cm to 2 cm. Such spectral indices are unusual but not unprecedented for SNRs. Since all sources discussed in this paper must be detected at 3.6 cm and 2 cm, selection effects will bias spectral indices to small values.

Active galactic nuclei (AGNs). It has been argued (Downes & Eckart 2007) that a supermassive black hole and an AGN are present within the western nucleus of Arp220. Radio emission from an AGN is likely present at some levels and so is potentially detectable. We would expect such an AGN associated compact source to be long-lived, but perhaps randomly variable in intensity. If as expected the radio emission arises within a jet then the spectrum should be flat (being generated from the superposition of synchrotron self-absorbed components peaking at different frequencies along the jet). Inspection of Figure 1 shows that the 3.6 cm images of the flat spectrum sources W33 and W42 could be consistent with a jet morphology. Both sources are long-lived and the first shows strong 18 cm variability. More observations, searching for structure and short-term variability, are needed to confirm the presence or absence of an AGN in Arp220.

Unclassified sources. Two of the sources, described in detail in the Appendix, namely, W39 and E10 have proved impossible to classify because they show declining luminosity at long wavelengths and increasing luminosity at short wavelengths, a behavior not predicted for any of the classes described above. More data are required on these sources.

4.2. *Flat Spectrum SNRs*

It was noted in Section 4.1 that the sources identified as SNRs mostly have flatter spectra than expected in standard models (with α = 0.5–0.7). Three alternative models could explain the origin of such flat spectra with spectral indices $\alpha \leqslant 0.5$. In one such model Schlickeiser & Fuerst (1989) argue that Fermi acceleration in strongly magnetized plasma flattens the electron injection spectrum ($\gamma \leqslant 2$) which consequently flattens the synchrotron emission spectrum giving $\alpha \leqslant 0.5$. In another model the intrinsic spectral index is $\alpha \simeq 0.5$ in the SNR shell but the overall spectrum appears flatter due to spatially variable free–free absorption. The integration over the whole SNR of local spectra with turnovers due to free–free absorption happening at different frequencies produces a flatter global spectrum. In the last model the presence of a plerion-like component with a flat or inverted spectrum in the center of the SNR results in an overall radio spectrum with spectral index $\alpha \leqslant 0.5$. Recent VLBI observations of SN1986J (Bietenholz & Bartel 2008) show the emergence of a new radio component in the center of the expanding radio shell. The new component shows an inverted radio spectrum contrasting with the power law plus free–free absorption turnover spectrum of the shell; the net result of this is to flatten the integrated spectrum. It is interesting that within Arp220 the spectrum of source W33 might be "double humped" (see Figure 4) showing a peak at ~2 GHz and another one at ~8 GHz. This is consistent with SN1986J like objects. Adding further to this interpretation, it is observed that both W33 and W42 have significantly smaller size at 2 cm than at 3.6 cm (see Section 3.2.3) which would be consistent with a compact central source being more dominant at higher frequency.

4.3. *Comparison of SNe and SNRs Sizes*

The top panel of Figure 5 plots the detected sources in the luminosity–diameter plane. This figure shows a clear difference in size between sources classified as SNRs (blue symbols) and SNe (red symbols). All six of the detected SNRs are resolved with diameter > 0.27 pc while all the SNe (except E14 which has size 0.30 pc) have sizes <0.2 pc. In normal galactic disks

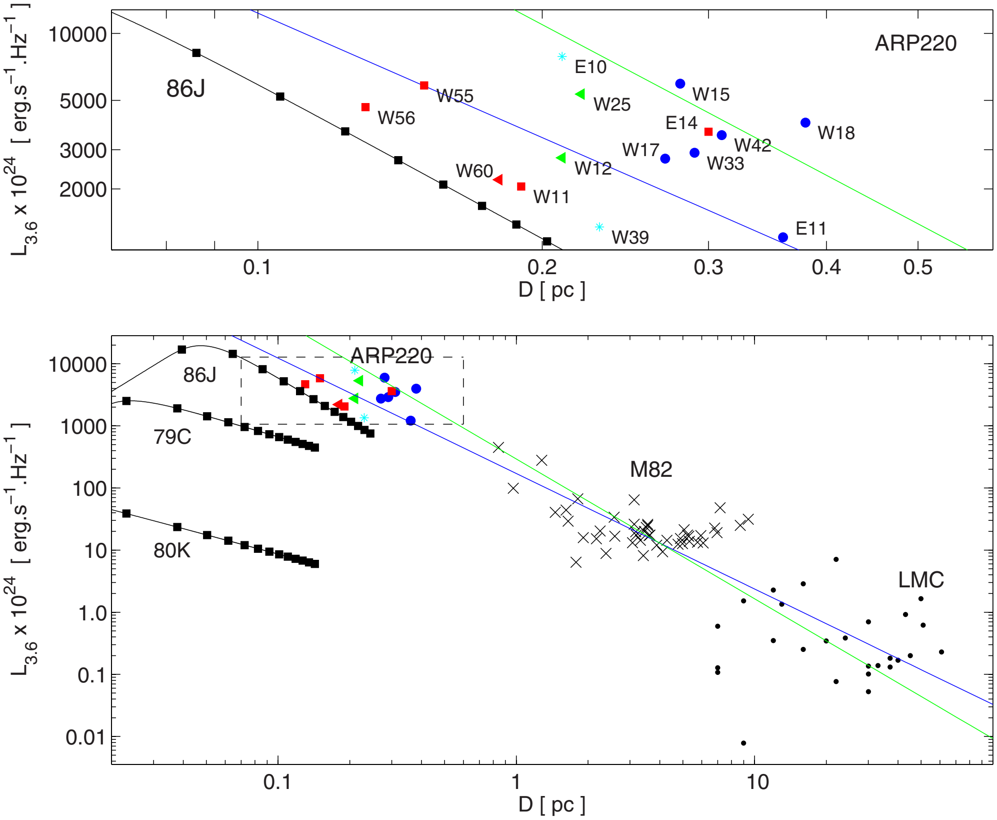

Figure 5. Illustration of the 3.6 cm flux densities and sizes of observed SNe and SNRs. The bottom panel plots sources in Arp220 and SNRs in M82 and the LMC. The top panel is a close-up view of the dashed rectangular region shown in the bottom panel showing only Arp220 sources. Red is used for sources identified as SNe, blue for sources identified as SNRs, green for possible transition objects, and cyan for unclassified sources. The SN tracks for SN1986J (Type IIn), SN1979C (Type IIL), and SN1980K (Type IIL) were produced using the light-curve fits given in Weiler et al. (2002) combined with the deceleration parameter from Bietenholz et al. (2002) for SN1986J and assuming free expansion at 10^4 km s^{-1} for both SN1980K and SN1979C. The square markers along each track indicate time evolution and are 1 year apart. Black crosses and dots show SNRs in M82 and the LMC. W34 and W58 are omitted as their size estimates are not considered dependable. In cases where a point is denoted by a triangle pointing left this signifies that the size estimate is an upper limit. In both panels the green line is the theoretical line of Berezhko & Völk (2004) of slope $-9/4$ while the blue line is the best fit through the SNR luminosities and sizes for all three galaxies. The data for the SNRs in M82 are taken from Huang et al. (1994) and the data for the SNRs in the LMC from Mills et al. (1984; see Section 4.6).

(A color version of this figure is available in the online journal.)

it has been argued (Chomiuk & Wilcots 2009) that the most compact/luminous SNR observed is determined by the age of the youngest SNR expected given the star formation rate. This mechanism cannot however explain the minimum size of SNRs in Arp220 because given the high predicted SN rate (4 ± 2 yr^{-1}) the above model predicts a much smaller limit than is observed. A physical minimum size is in fact expected because SNRs should first "switch on" and become luminous just as they enter their Sedov phase, which occurs when the swept up ISM mass equals the ejecta mass. The radius at which a source enters the Sedov phase therefore depends on the ISM density and the ejecta mass. Scoville et al. (1997) estimate in the western nucleus a mean molecular density of 1.5×10^4 cm^{-3}; more recently Sakamoto et al. (2008) estimate from gas dynamics a mean total mass density of $2 \times 10^3\ M_\odot$ pc^{-3} implying a gas molecular number density $< 4 \times 10^4$ cm^{-3}. Adopting a molecular ISM density of 10^4 cm^{-3} a minimum SNR diameter of 0.3 pc is expected, close to that observed. This cutoff size for SNRs goes only as the one-third power of the assumed ejecta mass and external density and so is only weakly dependent on these quantities. Despite this the sharpness of the observed minimum cutoff in size suggests that the observed Arp220 SNRs are not embedded in densities $> 10^5$ cm^{-3}. This is either because such high-density gas has low volume filling factor in Arp220 or because SNRs become inefficient radio sources (Wheeler et al. 1980) when embedded in such high-density regions.

In addition to a *minimum* size for SNRs we expect a *maximum* size for SNe set by the size of their wind-blown bubble. The predicted sizes of such bubbles are a function of the external ISM pressure, progenitor mass-loss rate, and wind velocity (see Equation (2) of Parra et al. 2007). The ISM pressure in Arp220 is estimated to be 10^7 K cm^{-3} (Dopita et al. 2005). The wind mass-loss rate and speed are expected to vary significantly between different progenitors. Weiler et al. (2002) estimates however that for the most powerful radio SNe (mostly Type IIn) mass-loss rates are $10^{-4}\ M_\odot$ yr^{-1} and velocities 10 km s^{-1}. Adopting these parameters gives an estimated wind-blown bubble diameter of 0.4 pc consistent with the upper limits on SNe sizes and comparable in size to our SNR diameters. It should be noted however that there is considerable uncertainty in the expected wind-blown bubble size since only the ratio of mass-loss rate and wind velocity is constrained by VLBI SN observations; and for a fixed ratio of these two quantities the bubble size is linearly dependent on the assumed wind velocity, a quantity which is poorly known. The fact that most of our observed SNe have size limits significantly smaller than 0.4 pc suggests that wind speeds could be 5 km s^{-1} or less.

In Section 4.1 we discuss the possibility of SN/SNR "transition objects" where interaction between the blast wave and the

ISM has started but the amount of mass accreted is still less than the ejecta mass. Such objects would be expected to be intermediate in size between SNe and SNRs. The two transition object candidates we have, W12 and W25, have estimated diameters <0.21 pc and <0.22 pc, respectively, which is consistent with a progenitor with a somewhat lower mass-loss rate/wind velocity or a slightly higher ISM pressure than assumed above.

It is notable that all of the SN candidates except one lie close together in the luminosity–size plane (see Figure 5). All these positions would be reached by the evolutionary tracks of SNe more radio luminous by approximately a factor of two than the well-studied Type IIn SN1986J (shown by the thick black line marked 86J in Figure 5). One SN classified source (E14) is however exceptional since it lies at a position in the luminosity–size plane more characteristic of SNRs. Such an intense SN source which is still highly luminous at late times when it has a large diameter (and hence likely peaked at an even higher luminosity), would not, however, be unprecedented. The radio supernova SN1982aa and gamma-ray bursts/SNe SN1998bw and SN2003w had 6 cm peak luminosities nearly 10 times larger than SN1986J (Chevalier 2006) and their evolutionary tracks would be consistent with the position of E14 in the luminosity–size plane.

4.4. *Source Expansion Velocities*

Supernovae. The majority of the SN identified sources have insufficient data to estimate their explosion dates and hence set limits on their expansion velocities. Three sources E14, W11, and W34 have however been detected at several 18 cm epochs showing close to linearly increasing flux densities with time (F. Batejat et al. 2012, in preparation). Compared to equivalent portions of the fitted 18 cm light curves for well-sampled radio SNe of similar luminosities, it seems that reasonable estimates of explosion dates (within accuracies of one year or so) can be made by linearly extrapolating the 18 cm light curves down to zero flux density and then subtracting a year. Applied to E14, W11, and W34, this algorithm gives ages, at the time of the 2 cm and 3.6 cm observations, of 7, 6, and 6 years, respectively. E14 is resolved at both 2 cm and 3.6 cm and W11 is provisionally resolved at 2 cm, allowing to measure their sizes with error bars. The size measurement of W34 we consider is unreliable and cannot be used to estimate an expansion velocity (see Section 3.2.3). Combining sizes and age estimates for the other two SNe we find that the E14 expansion velocity is in the range 13,700–28,000 km s^{-1} (90% confidence) and the W11 expansion velocity is in the range 7300–15,200 km s^{-1}. For the latter object the range is consistent with the canonical value of 10,000 km s^{-1} for a normal Type II SN. The velocity for E14 is somewhat larger than this but would not be exceptional. For instance VLBI observations of SN1993J (Marcaide et al. 1997) show it having a radio shell expansion velocity of 15,000 km s^{-1} at early times. Also Brunthaler et al. (2010) have recently measured an expansion velocity of ∼23,000 km s^{-1} for SN2008iz in M82.

Supernovae remnants. Of the six detected SNRs with measured sizes, four (W17, W18, W33, and W42) have been known since the original discovery observations of Smith et al. (1998) made in 1994. The remaining two sources, W15 and E11, have stable 18 cm light curves and spectra consistent with an SNR origin (see the Appendix) but with luminosities below the detection limit of the Smith et al. (1998) observations; these sources were very likely also present in 1994 but were not detectable. It seems highly probable that all the SNR identified sources are at least 12 years old. In fact 18 cm light-curve monitoring (see Figure 3 in Rovilos et al. 2005) shows their light curves declining relatively slowly so they are likely considerably older than this. Lonsdale et al. (2006) estimate ages of several decades. Our recent reanalysis of all the 18 cm monitoring data (F. Batejat et al. 2012, in preparation) agrees with this conclusion. Taking a rough estimate of their ages as 20 years and taking the mean diameter for this group of sources (0.31 pc) gives average expansion speeds since explosion of 5000 km s^{-1}. Such speeds are consistent with those expected for SNRs just entering the Sedov phase when the swept up ISM mass equals that of the ejecta so that strong deceleration is occurring.

Table 4
Magnetic Field and Energy Estimates

Source (1)	α (2)	Diameter (pc) (3)	B Rev (mG) (4)	E Part ($\times 10^{49}$ erg) (5)	E Part, DW ($\times 10^{49}$ erg) (6)
W15	0.72	0.28	23.4	3.3	3.5
W17	0.23	0.27	46.7	12.0	3.1
W18	0.62	0.38	19.9	6.0	4.8
W33	...	0.29	18.0	2.2	3.9
W42	0.24	0.31	49.7	20.4	4.4
E11	...	0.36	15.4	3.1	5.2
E14	0.72	0.30	20.9	3.3	4.0

Notes. Col. (1): source name. Col. (2): spectral index taken from Parra et al. (2007). The revised equipartition formula is not valid for spectral indices $\leqslant 0.5$. In cases where a source has $\alpha \leqslant 0.5$, i.e., sources W17 and W42, α is taken as 0.51. In cases where no spectral index information is available, i.e., sources W33 and E11, α is taken as 0.7. Col. (3): source diameter taken from Table 3. Col. (4): magnetic field derived using the revised equipartition formula of Beck & Krause (2005) adjusted to a magnetic field to particle energy ratio of 0.01. **K**, the ratio of number densities of cosmic-ray protons and electrons per particle energy interval within the energy range traced by the observed synchrotron emission is taken as 100. A shell inner to outer radius of 0.8 and a synchrotron filling factor of 10% are assumed. Col. (5): associated total energy in relativistic particles. Col. (6): total energy in relativistic particles estimated assuming energy density balance with ram pressure, expansion velocity from Draine & Woods (1991), a molecular number density of 10^4 cm^{-3}, and a synchrotron filling factor of 10%.

4.5. *Source Magnetic Fields and Energetics*

Given estimates of source sizes and synchrotron emission flux densities it is possible to work out minimum energies and equipartition magnetic fields. Most models of SNR evolution predict, however, that SNRs are far from equipartition and that energies are particle dominated. The Berezhko & Völk (2004) model assumes a 1% ratio of magnetic field to relativistic particle energy density. For the seven sources which are well resolved at two bands (comprising six SNR candidates and one SN candidate) we give in Table 4 estimates of magnetic fields and energies calculated assuming the revised magnetic field–relativistic particle equipartition expression of Beck & Krause (2005) adjusted to a 1% magnetic field to particle energy density ratio assumption. We assume a spherical shell geometry with a ratio of inner to outer radius of 0.8, an outer shell diameter given in Table 3 and an internal volume filling factor for radio emission of 10%. We also assume a ratio of proton to electron number density at fixed energy $\mathbf{K} = 100$ which according to Beck & Krause (2005) is valid for young SNRs. The results give magnetic fields in the range ∼15–50 mG and total energies in relativistic particles between 2% and 20% of the expected 10^{51} erg kinetic energy of a typical SN. This is consistent with estimates given by Lacki et al. (2010) for total particle energy fractions of relativistic particles needed to explain the FIR–radio correlation in compact starbursts via calorimeter models.

Consistency with the Berezhko & Völk (2004) model can be checked by comparing the particle energy in an SNR with the prediction that it should be $E_{\rm part} = \rho_{\rm ISM} v^2 V_{\rm shell}$, where $\rho_{\rm ISM}$ is the average density of the ISM, v is the SNR expansion velocity, and $V_{\rm shell}$ is the synchrotron-emitting volume of the SNR. This calculation assumes that ram pressure balances shell internal pressure which in turn is dominated by relativistic particles. Consistent with the latter assumption there is increasing observational evidence for a large/dominant fractional relativistic particle energy density in young SNRs (Patnaude & Fesen 2009; Berezhko et al. 2009). In Column 6 of Table 4, we give the estimated relativistic particle density given by the above ram pressure balance formula. A source-emitting volume $V_{\rm shell}$ was calculated from the measured source outer diameter assuming a shell with ratio of inner to outer radius of 0.8 with synchrotron filling factor of 10%. The ram pressure $\rho_{\rm ISM} v^2$ was calculated from velocities given by Draine & Woods (1991) for SNRs of the size observed in a medium of density 10^4 cm^{-3}; note however that this estimate is only weakly dependant on the assumed ISM density since in the Sedov phase the predicted expansion velocity scales as $\rho^{-0.5}$ for fixed diameter. As expected during the Sedov phase the estimated particle energies in Column 6 of Table 4 are close to a constant. We find that these estimated relativistic particle energies are in good agreement with those in Column 5 derived from the measured synchrotron flux densities assuming a 1% ratio of magnetic to particle energy density.

Estimates of source magnetic fields are given in Column 4 of Table 4, as derived from the measured source radio luminosities and sizes assuming a 1% magnetic to relativistic particle energy density ratio and the source geometry and synchrotron volume filling factor described above. Thompson et al. (2009) estimate somewhat smaller field values, averaging 9 mG for the sources listed in Table 4. These published estimates were made without the benefit of knowing the source sizes by assuming that 1% of the total kinetic energy of 10^{51} erg goes into relativistic electrons and finding the magnetic field that gives the observed source radio synchrotron luminosity (νL_ν). It was argued that these relatively modest fields could be produced by shock compression of ISM fields of a few mG, fields sufficiently strong to explain the IR–radio correlation via calorimeter models, even in the presence of inverse Compton energy losses off ambient starlight photons (Thompson et al. 2009). This compression model predicts, however, that SNRs have constant radio intensities until the electron synchrotron energy loss time ($\geqslant$200 years at 5 GHz for the sources in Arp220). Most observable sources would then be older than 100 years old and therefore be larger than 0.7 pc in diameter in a 10^4 cm^{-3} density medium (Draine & Woods 1991), a factor two greater than their measured sizes. An additional consequence of such a model, given the high SN rate in Arp220, is that many more SNR sources than the six candidates presented in this paper would be expected to be detected (order of a few hundred). The low number of observed SNRs in Arp220 combined with their small sizes argue against models in which SNR magnetic fields are generated from compressed ISM magnetic fields.

4.6. The SNR Luminosity–Size Relation

A correlation between the radio surface brightness (Σ) of SNRs and their diameters (D) has long been claimed (Shklovskii 1960). Such a correlation can alternatively be cast as one between radio luminosity (L) and diameter (D), a formulation which removes the implicit D^{-2} correlation automatically induced by plotting Σ. Both the reality and slope of the correlation has been a controversial topic given the likelihood of strong selection effects, both in our Galaxy (Green 2005) and (to a lesser extent) in external galaxies (Urošević et al. 2005). It has also been claimed that if the $\Sigma - D$ and L–D correlations exist, they are secondary correlations due to correlations with the ISM density (Berkhuijsen 1986; Bandiera & Petruk 2010). Finally, it has been claimed (Arbutina & Urošević 2005) that different correlations exist for the luminous SNRs in galactic dense clouds and most observed extragalactic SNRs compared to galactic SNRs in low-density regions.

We can test the claimed L–D correlation for powerful SNRs by comparing the diameters and luminosities of the SNRs in Arp220 with those found in M82 and the LMC (see bottom panel of Figure 5). The data for 45 SNRs in M82 used in Figure 5 are taken from Huang et al. (1994) who use the FWHM of a Gaussian fit as an estimate of source diameter. To make these estimates compatible with our Arp220 estimates we have converted this to a dispersion and then to the diameter of a shell model with ratio of inner to outer radius 0.8. The data for the LMC are taken from Mills et al. (1984). These authors obtained sizes by taking two models, one comprising a thin circular ring and another a uniform circular disk and fitting to the half power response along the major and minor axes. An average of the two values is chosen and is expected to give a reasonable approximation to the shell size as defined for Arp220.

Figure 5 clearly shows that the data for Arp220 are to first order consistent with an extension of the L–D correlation to very small size SNRs. More quantitatively an unweighted least-squares fit to all SNR points gives the best-fitting relation $L \propto D^{-1.9}$ (drawn in blue in Figure 5). This gradient is, however, mostly determined by the M82 and LMC data because of the larger number of SNRs plotted for these galaxies.

Models for radio SNR evolution such as those presented by Huang et al. (1994) and Berezhko & Völk (2004) posit constant ratios between relativistic particles and field energy densities and roughly constant energy in relativistic particles during the Sedov phase. Individual SNRs evolve along the luminosity–diameter correlation during their Sedov phase on tracks which are independent of the external density $n_{\rm ISM}$ (Berezhko & Völk 2004).[6] Assuming an optically thin radio synchrotron spectral index of 0.5, these models predict $L \propto D^{-9/4} E^{7/2}$, where E is the SN kinetic energy. Assuming that all SNe have close to the same energy then we expect $L \propto D^{-9/4} = D^{-2.25}$. Assuming this dependence and fitting the constant of proportionality we obtain the green line in Figure 5. This theoretical correlation fits the observed Arp220 data very well and also, given their large internal scatter, is consistent with the M82 and LMC data.

Some competing models argue that radio SNR luminosity is instead mostly determined by ISM density with source size being of secondary importance. In one such model (van der Laan 1962; Thompson et al. 2009) the internal magnetic fields that control SNR luminosity are compressed ISM fields which themselves increase with ambient density ($B_{\rm ISM} \propto n_{\rm ISM}^{\alpha}$) giving

---

[6] Despite this direct independence of L on $n_{\rm ISM}$ these models can explain that the most luminous SNRs are found in host nuclei with high densities such as Arp220 because (1) such nuclei have the highest star formation rates and hence the youngest, smallest diameter, and so most luminous SNRs (Chomiuk & Wilcots 2009) and because (2) there is a minimum "switch on" size for Sedov phase SNRs, which decreases as density increases, increasing the maximum SNR luminosity.

rise to a L–$n_{\rm ISM}$ relation. A secondary L–D relation can however still occur because the diameter of typically observed SNRs also depends on ISM density. Specifically in the model of van der Laan (1962) the radio luminosity of an SNR at a given frequency stays roughly constant till a time equal to the electron synchrotron loss time, $t_{\rm syn}$ after which it rapidly declines. Given that SNRs are decelerating during their Sedov and subsequent pressure-driven snow-plow phases it follows that most observed radio SNRs in a flux-limited sample will have sizes close to their sizes at the synchrotron loss time $t_{\rm syn}$. For most sources plotted in Figure 5 the predicted $t_{\rm syn}$ is comparable or larger than the age and which they enter the snow-plow phase for which $D \propto n_{\rm ISM}^{-1/7} t_{\rm syn}^{2/7}$ (McKee & Ostriker 1977); substituting $t_{\rm syn} \propto B_{\rm ISM}^{-3/2}$ and $B_{\rm ISM} \propto n_{\rm ISM}^{\alpha}$ a D–$n_{\rm ISM}$ relationship results. Combining this with the predicted L–$n_{\rm ISM}$ relationship noted earlier we find that we get an L–D relationship with power-law exponent of -2.25 if the power-law exponent linking ISM magnetic field and density has a value $\alpha = 0.6$.

Thompson et al. (2009) assuming the van der Laan (1962) SNR model have estimated $B_{\rm ISM}$ in a number of galaxies and have compared this to estimates of ISM surface density Σ finding the empirical relation (Thompson et al. 2009, Equation (6)) $B \propto \Sigma^{0.55}$. If one assumes a constant gas scale height then $n \propto \Sigma$ and $B_{\rm ISM} \propto n^{0.55}$; similar to the value of the exponent required above to explain the slope of the L–D relation. Despite this consistency there is no physical explanation of why the exponent value is 0.55.[7] In contrast the model of Berezhko & Völk (2004) directly predicts the slope of the observed L–D from the model's assumed physics. Additionally in Section 4.5 we gave arguments based on source energetics, sizes, and numbers that the Berezhko & Völk (2004) model applies in Arp220. The fact that the Berezhko & Völk (2004) model naturally explains the L–D relation *between* galaxies and that all galaxies fall on the same L–D relation argues that this is the only mechanism needed and that it also applies in M82 and the LMC. The Berezhko & Völk (2004) model in normal galaxies is also favored by the work on SNR luminosity functions by Chomiuk & Wilcots (2009).

A strong test which can differentiate between density-dependent models and the Berezhko & Völk (2004) model would be to look for the time variations in luminosity predicted to occur only in the latter model as individual sources expand and move along the L–D correlation. Given the small sizes of the SNR sources in Arp220 quite large flux variations are expected over relatively short times. For instance if our SNRs are expanding at 3000 km s^{-1} just as they enter the Sedov phase, then for a diameter $\sim$0.3 pc they increase in diameter by 2% yr^{-1} which from Berezhko & Völk (2004) implies a flux density decrease of 4.8% yr^{-1}. Rovilos et al. (2005), who analyzed five epochs of 18 cm data spanning 5.6 years, were able to rule out factor of two variations over that period, as expected from SNe models, but not variations of the amplitude predicted above. We are presently analyzing nine 18 cm data sets over a longer time period to see if we can detect the predicted flux density decline.

4.7. *ISM Magnetic Fields in Arp220*

In Sections 4.5 and 4.6 we argue that in SNRs internally generated magnetic fields dominate over compressed ISM magnetic fields both in Arp220 and other galaxies. The compressed ISM magnetic field contribution must therefore be significantly less than our total estimated internally generated field, i.e., $f\, B_{\rm ISM} \ll B_{\rm SNR}$, with f ranging from 3 to 6 for young SNRs (Völk et al. 2002). Taking the median $B_{\rm SNR}$ from Table 4 we get an upper limit on $B_{\rm ISM}$ ranging from 3.5 mG to 7 mG in Arp220. This is consistent with the estimates of magnetic fields from OH maser Zeeman splitting (0.7–4.7 mG; Robishaw et al. 2008). For comparison Thompson et al. (2009) estimate a minimum ISM magnetic field of $\sim$1 mG in order that synchrotron emissivity dominates over inverse Compton losses. Thompson et al. (2009) also estimate an upper limit of 20 mG based on the argument that the magnetic field is dynamically lower than gravity.

5. CONCLUSIONS

The main conclusions of this paper are as follows.

1. We have detected two new sources at both 2 cm and 3.6 cm wavelength in the western nucleus of Arp220, namely, W58 and W60.
2. We have resolved for the first time, 11 of the 17 detected sources at 2 cm, 8 at 3.6 cm, and 7 at both 2 cm and 3.6 cm.
3. We confirm the claim of Parra et al. (2007) that the compact radio sources in Arp220 mostly comprise a mixed population of SNe and SNRs. Two sources are candidate SN/SNR transition objects. A few sources remain difficult to classify and may be AGN components. Ongoing VLBI monitoring at 6 cm should shed further light on the nature of these sources.
4. The sources resolved at both wavelengths (all but one of which are SNRs) have diameters in the range 0.27–0.38 pc with mean 0.31 pc. In comparison the SNe are, except in one case (E14), all unresolved. The observed size boundary between SNe and SNRs is consistent with an ISM density of $\sim 10^4$ cm^{-3}.
5. Combining source sizes with source ages enables us to calculate upper limits for source expansion velocities averaged over their lifetime. We find expansion velocities $<$30,000 km s^{-1} for the SNe W11 and E14 and $\sim$5000 km s^{-1} for the SNRs.
6. We argue that magnetic fields in the SNRs of Arp220 are internally generated (Berezhko & Völk 2004) and not dominated by compressed ISM magnetic fields (van der Laan 1962). This interpretation is supported by the fact that the particle energy density estimated from synchrotron fluxes and sizes, assuming a 1% ratio of magnetic field to relativistic particle energy density ratio, is equal to the ram pressure energy density, just as predicted by Berezhko & Völk (2004). Furthermore the relativistic particle total energies are consistent with values required to fit the FIR–radio correlation (Lacki et al. 2010). In contrast the compressed field model is inconsistent with the low number of observed SNRs and their small measured diameters.
7. The observed SNR radio luminosity as a function of diameter for sources in Arp220, M82, and the LMC is in good agreement with the predicted relation $L_\nu \propto D^{-2.25}$ as derived assuming internally generated magnetic fields in SNR shells (Berezhko & Völk 2004).
8. Based on our conclusion that in SNRs internal magnetic fields dominate over compressed ISM magnetic fields we estimate an upper limit of 7 mG for the ISM magnetic field in Arp220. This is consistent with other estimates and limits.

---

[7] Thompson et al. (2009) instead argue that physically $B_{\rm ISM} \propto n$ might be expected based on equipartition between the magnetic field energy density and the energy density required to balance disk gravity.

This research was partly supported by the EU Framework 6 Marie Curie Early Stage Training programme under contract number MEST-CT-2005-19669 "ESTRELA." J.C. acknowledges funding from a Swedish VR research grant. The European VLBI Network is a joint facility of European, Chinese, South African, and other radio astronomy institutes funded by their national research councils. The National Radio Astronomy Observatory is a facility of the National Science Foundation operated under cooperative agreement by Associated Universities, Inc. The authors thank the staff at NRAO and JIVE for their diligent correlation of the data and the referee whose comments helped improve the paper.

APPENDIX

This appendix assigns source type classifications (mostly SN or SNR) to the high-frequency detected sources in Arp220. In Section 4.1 we discuss the expected temporal and spectral properties of each of the possible source classes. The most critical information for classification is the variability properties of each source. Concentrating on recent high sensitivity data we find that source variability properties fall naturally into four different groups which we term "rapidly rising," "possibly rising," "stable," and "possibly declining." The term "rapidly rising" is used in the individual source descriptions below at 18 cm and 6 cm for a source whose flux density has risen more than 3σ and 30%, between two high sensitivity epochs over ∼2.5 years (comparing the two 6 cm epochs in Table 2 and the 2003.85 and 2006.44 epochs at 18 cm). The same term is used at 3.6 cm for a source whose flux density has risen by more than 3σ and 15% over the 0.89 years between the two epochs. The term "possibly rising" is used for a source whose flux density has risen by more than 1σ and the term "possibly declining" is used for a source whose flux density has declined by more than 1σ. The term "stable" is used for any variation in flux density lower than 1σ.

W11. First detected at 18 cm in epoch 2003.85 this source is rapidly rising at 18 cm. It is also rapidly rising at 6 cm and stable at 3.6 cm. Its spectrum peaks around 3 GHz. We classify W11 as an SN.

W12. First detected at 18 cm in epoch 2002.88 this source is rapidly rising at 18 cm and 6 cm. A similar rise rate at 3.6 cm is consistent with the data. The radio spectrum shows a straight power-law spectrum from 18 cm to 3.6 cm. We classify this source as a candidate SN/SNR transition object.

W15. First detected at 18 cm in epoch 2002.88. Parra et al. (2007) classified this source as ambiguous because it was detected in the 18 cm observations GD17A and GD17B but at levels below the Rovilos et al. (2005) sensitivity limit, meaning that it could be either a new source or a long-lived stable source not detected earlier because of sensitivity limitations. Subsequent data, showing a stable 18 cm light curve, are more consistent with the latter interpretation. However, a possible rise at both 6 cm (16%) and 3.6 cm (18%) may be in contradiction with an SNR origin. Despite this, considering potential ∼10% calibration/reconstruction uncertainties, the large size of this object (0.28 pc resolved at both 6 cm and 3.6 cm bands) and its spectrum peaking around 3 GHz, we provisionally classify W15 as an SNR.

W17. A long-lived source discovered by Smith et al. (1998). Its long-term 18 cm light curve is stable and its 6 cm and 3.6 cm light curves are possibly declining. Its spectral shape is quite flat but could be interpreted as being double humped with one peak at ∼1.5 GHz and another at ∼5 GHz. We classify W17 as an SNR.

W18. A long-lived source first discovered by Smith et al. (1998). Long-term 18 cm flux density monitoring shows a steady decrease of 8% yr^{-1} over 11.6 years. In more recent shorter wavelengths at 6 cm and 3.6 cm the source is classified, respectively, as possibly declining and possibly rising. W18's spectrum turns over around 3 GHz. We provisionally classify W18 as an SNR. This classification is based primarily on its long-lived nature and declining light curves at 18 cm and 6 cm.

W25. First observed at 18 cm in epoch 2002.88. It is rapidly rising at 18 cm, 6 cm, and 3.6 cm. Its spectra peak around 3 GHz. Primarily based on its rapidly rising light curves at all frequencies we consider this source to be a candidate SN/SNR transition object.

W33. A long-lived source first discovered in Smith et al. (1998). Its 18 cm and 6 cm light curves are possibly declining over ∼2.5 years while its 3.6 cm flux density has remained stable over 0.89 years. On average its 18 cm flux density has decreased ∼10% yr^{-1} since monitoring began in 1994. The spectrum of W33 is quite flat with hints of two broad peaks at ∼2 GHz and ∼8 GHz. Parra et al. (2007) suggested that W33 is a possible AGN candidate. Inspection of the 3.6 cm image of W33 does not exclude the possibility of a jet morphology. Based on the behavior of its multifrequency light curves we provisionally classify W33 as an SNR but an AGN origin is still possible.

W34. First discovered at 18 cm in epoch 2003.85. This was followed by a rapid rise at 18 cm epochs. W34's 6 cm light curve is also rapidly rising while the source is stable at 3.6 cm. W34's spectrum turns over around 5 GHz. The light curves and spectrum are consistent with it being an SN.

W39. A long-lived source detected by Smith et al. (1998). Long-term monitoring shows a steady decline at 18 cm (∼7% yr^{-1}). From recent short wavelength data it is classified as stable at 6 cm and possibly rising at 3.6 cm. The source's spectrum turns over at ∼2 GHz. Given its unusual multifrequency variability properties (declining at long wavelengths but stable or rising at short wavelengths) we refrain from speculation about the nature of W39 until more data are available.

W42. A long-lived source first detected by Smith et al. (1998). It has decreased by less than 8% in 18 cm flux density since 1994 while its recent 6 cm and 3.6 cm light curves are stable. W42 is the most stable of the long-lived sources. The spectrum is quite flat from 18 cm to 3.6 cm. There is no sign of a low-frequency turnover but there is a high-frequency turn down from 3.6 cm to 2 cm. We conclude that W42 is likely to be an SNR.

W55. First detected at high frequency by Parra et al. (2007) in epoch 2006.02. No 18 cm data are available. The source's 3.6 cm light curve is possibly declining, the 6 cm light curve is rapidly declining and its spectrum peaks at around 8 GHz. We provisionally classify W55 as an SN.

W56. This source was first discovered by Parra et al. (2007) in epoch 2006.02. No 18 cm data are available. The source is rapidly rising at 6 cm and stable at 3.6 cm. W56's spectrum turns over around 5 GHz. Considering these properties we conclude that W56 is an SN.

W58. A newly detected source in the most recent 2 cm and 3.6 cm observations. At these two wavelengths it has flux densities of 226 and 322 μJy, respectively. At this 3.6 cm flux density the source would have been less than a $4\sigma_{\mathrm{rms}}$ detection in BP129 (epoch 2006.02). New 6 cm data from GC031A yield a flux density of 723 μJy. Re-reduction of BP129 6 cm data made it possible to clearly detect this source at epoch 2006.02 with a flux density of 408 μJy (not detected by Parra et al. 2007) allowing us to classify it as rapidly rising (77% increase in ~2.5 years). No 18 cm or 3.6 cm light-curve information is available. We classify W58 as an SN.

W60. A newly detected source in the most recent 2 cm and 3.6 cm observations. The source was also detected in the latest 6 cm observation in experiment GC031A (epoch 2008.44) at a flux density of 1016 μJy. Re-reduction of BP129 6 cm data made it possible to clearly detect this source at epoch 2006.02 with a flux density of 285 μJy (not detected by Parra et al. 2007) allowing us to classify this source as rapidly rising at 6 cm. We classify W60 as an SN.

E10. First detected at 18 cm in epoch 2002.88. It showed a decline in the next epoch and was undetectable in the last two 18 cm epochs. The source spectrum peaks at ~5 GHz. This observed fast low-frequency decline is too rapid to be consistent with an SNR and suggests instead a rapidly evolving Type Ib/c SN observed after its peak at 18 cm. However, in contradiction to this interpretation the source is rapidly rising at 6 cm and 3.6 cm. We leave E10 unclassified until further data are available.

E11. First detected in the high sensitivity 18 cm epoch 2002.88 at a flux density below the detection limit of earlier epochs. Its 18 cm flux density has decreased by less than 4% in subsequent 18 cm monitoring spanning ~3.5 years. It was not detected by Parra et al. (2007) at 6 cm and 3.6 cm. Re-reduction of BP129 6 cm data (epoch 2006.02) made it possible to clearly detect this source with a flux density of 429 μJy compared to 310 μJy in experiment GC031A (epoch 2008.44) allowing us to classify it as possibly declining at this wavelength. Based on its stable 18 cm light curve and possibly declining 6 cm light curve we classify E11 as an SNR.

E14. First detected at 18 cm in epoch 2002.88. In subsequent monitoring it shows a rapidly rising 18 cm light curve over ~2.5 years. The source is classified as possibly declining at 6 cm and stable at 3.6 cm. The spectrum shows a turnover frequency at 2 GHz. We classify E14 as an SN.

REFERENCES

Arbutina, B., & Urošević, D. 2005, MNRAS, 360, 76
Bandiera, R., & Petruk, O. 2010, A&A, 509, 34
Beck, R., & Krause, M. 2005, Astron. Nachr., 326, 414
Berezhko, E. G., Ksenofontov, L. T., & Völk, H. J. 2009, A&A, 505, 169
Berezhko, E. G., & Völk, H. J. 2004, A&A, 427, 525
Berkhuijsen, E. M. 1986, A&A, 166, 257
Beswick, R. J., Riley, J. D., Martí-Vidal, I., et al. 2006, MNRAS, 369, 1221
Bietenholz, M. F., & Bartel, N. 2008, Adv. Space Res., 41, 424
Bietenholz, M. F., Bartel, N., & Rupen, M. P. 2002, ApJ, 581, 1132
Brunthaler, A., Martí-Vidal, I., Menten, K. M., et al. 2010, A&A, 516, A27
Burrows, C. J., Krist, J., Hester, J. J., et al. 1995, ApJ, 452, 680
Chevalier, R. 2006, arXiv:astro-ph/0607422
Chomiuk, L., & Wilcots, E. M. 2009, ApJ, 703, 370
Dopita, M. A., Groves, B. A., Fischera, J., et al. 2005, ApJ, 619, 755
Downes, D., & Eckart, A. 2007, A&A, 468, L57
Draine, B. T., & Woods, D. T. 1991, ApJ, 383, 621
Fenech, D., Beswick, R., Muxlow, T. W. B., Pedlar, A., & Argo, M. K. 2010, MNRAS, 408, 607
Fenech, D. M., Muxlow, T. W. B., Beswick, R. J., Pedlar, A., & Argo, M. K. 2008, MNRAS, 391, 1384
Green, D. A. 2005, Mem. Soc. Astron. Ital., 76, 534
Huang, Z. P., Thuan, T. X., Chevalier, R. A., Condon, J. J., & Yin, Q. F. 1994, ApJ, 424, 114
Kronberg, P. P., Biermann, P., & Schwab, F. R. 1985, ApJ, 291, 693
Lacki, B. C., Thompson, T. A., & Quataert, E. 2010, ApJ, 717, 1
Lenc, E., & Tingay, S. J. 2009, AJ, 137, 537
Lonsdale, C. J., Diamond, P. J., Thrall, H., Smith, H. E., & Lonsdale, C. J. 2006, ApJ, 647, 185
Marcaide, J. M., Alberdi, A., Ros, E., et al. 1997, ApJ, 486, L31
Martí-Vidal, I., Marcaide, J. M., Alberdi, A., et al. 2011, A&A, 526, A142
McKee, C. F., & Ostriker, J. P. 1977, ApJ, 218, 148
Mills, B. Y., Turtle, A. J., Little, A. G., & Durdin, J. M. 1984, Aust. J. Phys., 37, 321
Morris, T., & Podsiadlowski, P. 2007, Science, 315, 1103
Muxlow, T. W. B., Pedlar, A., Wilkinson, P. N., et al. 1994, MNRAS, 266, 455
Parra, R., Conway, J. E., Diamond, P. J., et al. 2007, ApJ, 659, 314
Patnaude, D. J., & Fesen, R. A. 2009, ApJ, 697, 535
Pérez-Torres, M. A., Romero-Cañizales, C., Alberdi, A., & Polatidis, A. 2009, A&A, 507, L17
Petrov, L., Kovalev, Y. Y., Fomalont, E., & Gordon, D. 2005, AJ, 129, 1163
Pradel, N., Charlot, P., & Lestrade, J.-F. 2006, A&A, 452, 1099
Robishaw, T., Quataert, E., & Heiles, C. 2008, ApJ, 680, 981
Rovilos, E., Diamond, P. J., Lonsdale, C. J., Smith, H. E., & Lonsdale, C. J. 2005, MNRAS, 359, 827
Sakamoto, K., Wang, J., Wiedner, M. C., et al. 2008, ApJ, 684, 957
Schlickeiser, R., & Fuerst, E. 1989, A&A, 219, 192
Scoville, N. Z., Yun, M. S., & Bryant, P. M. 1997, ApJ, 484, 702
Shklovskii, I. S. 1960, SvA, 4, 355
Smith, H. E., Lonsdale, C. J., Lonsdale, C. J., & Diamond, P. J. 1998, ApJ, 493, L17
Thompson, T. A., Quataert, E., & Murray, N. 2009, MNRAS, 397, 1410
Ulvestad, J. S. 2009, AJ, 138, 1529
Urošević, D., Pannuti, T. G., Duric, N., & Theodorou, A. 2005, A&A, 435, 437
van der Laan, H. 1962, MNRAS, 124, 125
Völk, H. J., Berezhko, E. G., Ksenofontov, L. T., & Rowell, G. P. 2002, A&A, 396, 649
Weiler, K. W., Panagia, N., Montes, M. J., & Sramek, R. A. 2002, ARA&A, 40, 387
Wheeler, J. C., Mazurek, T. J., & Sivaramakrishnan, A. 1980, ApJ, 237, 781
Zanardo, G., Staveley-Smith, L., Ball, L., et al. 2010, ApJ, 710, 1515